Geophysics Research Letter

Supporting Information for

Unrest Detected at Socompa Volcano, Northern Chile, from Geodetic Observations

F. Liu[1], J. R. Elliott[1], S. K. Ebmeier[1], T. J. Craig[1], A. Hooper[1], C. Novoa Lizama[1], and F. Delgado[2]

[1]COMET, School of Earth and Environment, University of Leeds, Leeds, United Kingdom

[2]Department of Geology and Centro de Excelencia en Geotermia Andina, Universidad de Chile, Santiago, Chile

Contents of this file

Additional Supporting Information (Files uploaded separately)

Introduction

Text S1. InSAR processing details

We use the LiCSAR processing chain to form interferograms with multilooking (4 in azimuth and 20 in range), but no further spatial filtering, using Sentinel-1 Interferometric Wide (IW) swath mode Single Look Complex (SLC) images and the Digital Elevation Model (DEM) from the Shuttle Radar Topography Mission (SRTM) 1 arcsec. We form interferogram networks by connecting each image to 10 subsequent acquisitions (6-60 days temporal interferogram, assuming revisiting time is 6 days). We then use the StaMPS software to perform time series analysis, which includes a) resampling pixels to 500 m resolution to reduce data volume, b) application of GACOS correction for tropospheric artefacts using the TRAIN software (Bekaert et al., 2015), c) unwrapping iteratively to reduce unwrapping errors by checking for phase consistency (Hussain et at., 2016), and finally d) using only longer temporal interferograms (48-60 days) for the small baseline inversion to reduce the potential impact of the fading signal (Ansari et al., 2020; Maghsoudi et al., 2022; Purcell et al., 2022).

Text S2. GPS vector decomposition

We can decompose any vectors in a two-dimensional space into two orthogonal vectors. Considering the GPS horizontal displacement, we have the conventional orthogonal coordinates of North and East components, to indicate the GPS position. It is also possible to decompose an arbitrary GPS observation into another orthogonal coordinate system instead of the North-East one. As the figure shown here, we could decompose the vector $\mathbf{V_3}$, an arbitrary observation, into the $\mathbf{V_1}$ (displacement parallel to the direction of seasonal motion), and $\mathbf{V_2}$ (displacement perpendicular to the direction of seasonal motion) coordinates.

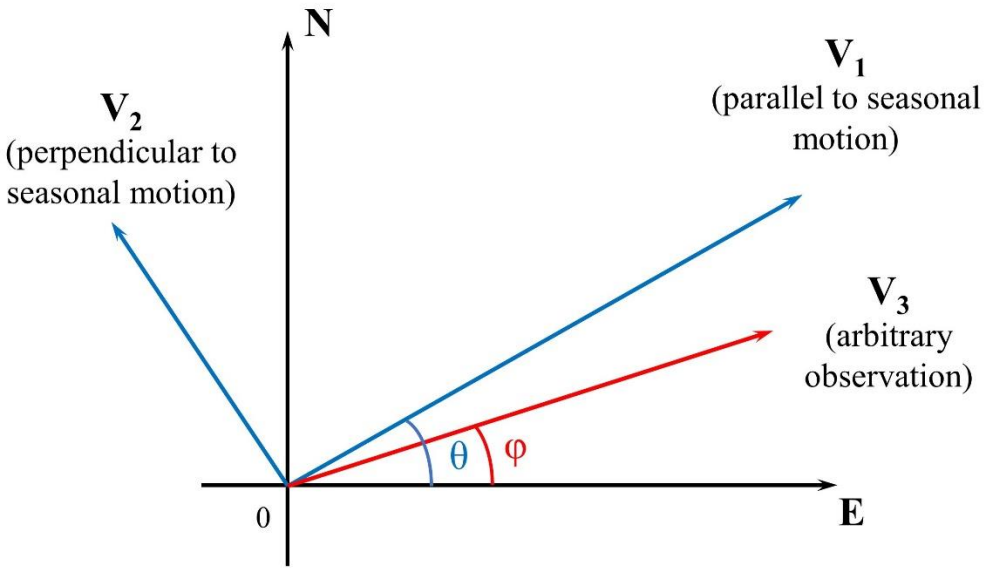

After the decomposition, we have

$$\delta_1 = |\boldsymbol{V_3}|\cos(\theta - \varphi)$$
$$\delta_2 = |\boldsymbol{V_3}|\sin(\theta - \varphi)$$

where δ_1 and δ_2 represent the displacement parallel and perpendicular to the direction of seasonal motion, respectively, θ is the angle between $\mathbf{V_1}$ and $\mathbf{E}$, and φ is the angle between $\mathbf{V_3}$ and $\mathbf{E}$.

Since the direction of seasonal displacement varies throughout the year, to determine the angle θ, we calculate the seasonal direction at time t using the following equation:

$$\theta(t) = tan^{-1}\left(\frac{|\boldsymbol{N}(t)|}{|\boldsymbol{E}(t)|}\right)$$

As the first three years of the horizontal GPS time series of the SOCM site are dominated by seasonal signals, we first calculate θ for each day in the first three years, then average the results of the three years, and finally get the value of θ on each day throughout a year. After obtaining the seasonal direction, we then decompose the horizontal GPS time series into the displacement parallel and perpendicular to the direction of seasonal motion.

Text S3. Tying InSAR and GNSS observation

Here we use all available continuous GPS sites from the database of the Nevada Geodetic Laboratory (Figure S10). We adopt the linear velocity calculated by the Nevada Geodetic Laboratory, using South America Plate as the reference frame.

We first derive the InSAR velocity map from the time series data, and average the values of the pixels surrounding the GPS sites (a circle with a radius of 3 km centred on it, ~120 pixels) as the corresponding velocity value of InSAR data. We then remove a spatial linear ramp in the east and north direction from the InSAR velocity map to minimize the relative difference between InSAR and GNSS, on ascending and descending respectively. Finally, based on this deramped InSAR velocity map and assuming no deformation signals on the north component, we can obtain the uplifting velocity of any pixels that are covered by both tracks by decomposing the InSAR velocity map into the east-west and vertical direction by solving the following formula:

$$\begin{bmatrix} U_{asc} & E_{asc} \\ U_{dsc} & E_{dsc} \end{bmatrix} \begin{bmatrix} V_U \\ V_E \end{bmatrix} = \begin{bmatrix} V_{asc} \\ V_{dsc} \end{bmatrix}$$

where *U* and *E* are the up and east components of the line of sight (LOS) vector, respectively.

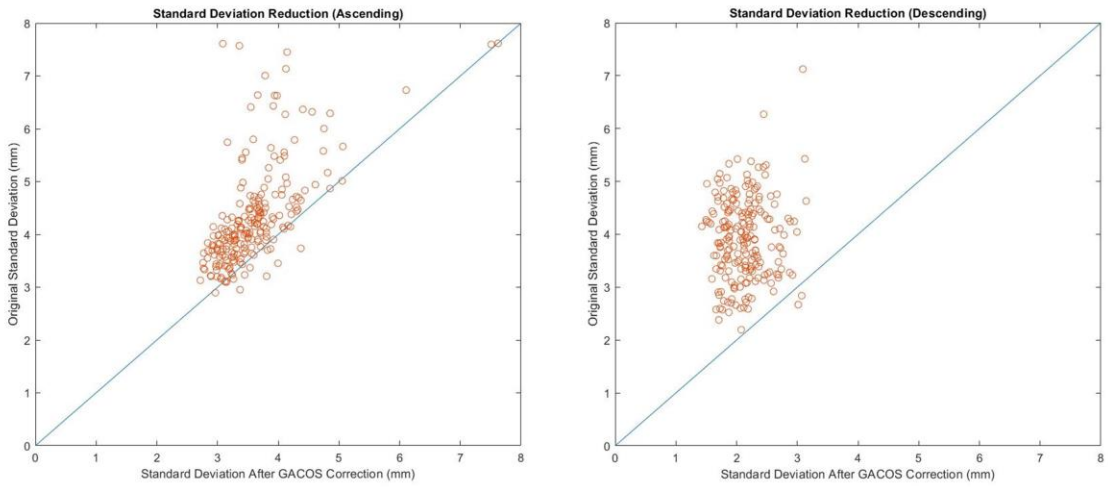

Figure S1. Standard deviation reduction of interferograms after the GACOS correction on ascending and descending track data, respectively. The red dots represent each epoch on time series, and the blue line is the identity line where any dots above it means an improvement after the GACOS correction. Here the average standard error reductions are 16.9% and 45.7% for ascending and descending, respectively.

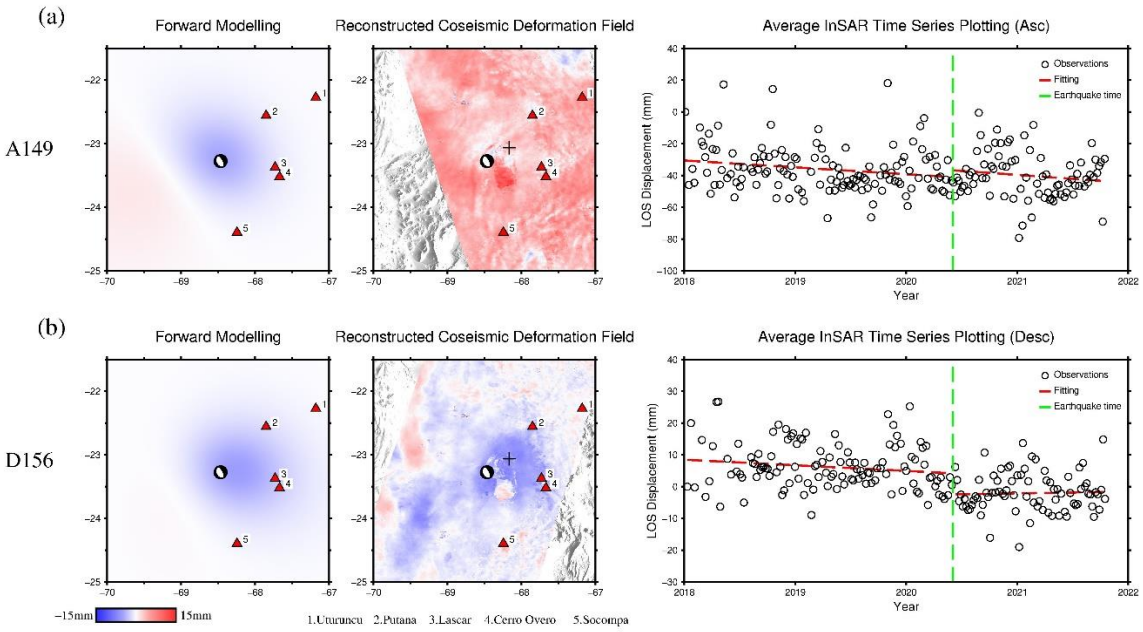

Figure S2. Coseismic deformation field of the M_w 6.8 earthquake reconstruction by InSAR time series fitting. (a) Data of ascending track. From left to right, the forward modelling from the USGS solution (strike: 332°, Dip: 59°, Rake: -94°, centroid depth: 112 km, Moment: 2.29×10^{19} N-m), the reconstructed coseismic deformation field, and the average InSAR time series of peak displacement pixels. (b) Same as (a) but for the descending track. For the forward modelling, we assume a uniform dislocation embedded in an isotropic elastic half-space, faults are equal in width and length, the slip-to-length ratio is set to 1.5×10^{-5} for this interplate earthquake, and the rigidity value used here for moment calculation is 75 GPa. The epicentre of the earthquake is indicated by the black focal mechanism, and volcanoes are marked by red triangles. On the reconstructed coseismic deformation field, the location of peak displacement pixels is marked by a plus symbol. The red patch close to the southeastern point of the epicentre marked (which is observed on both tracks) indicates the shape of Salar de Atacama, and has different behaviour in the time series. In all figures, positive values mean movements towards the satellite.

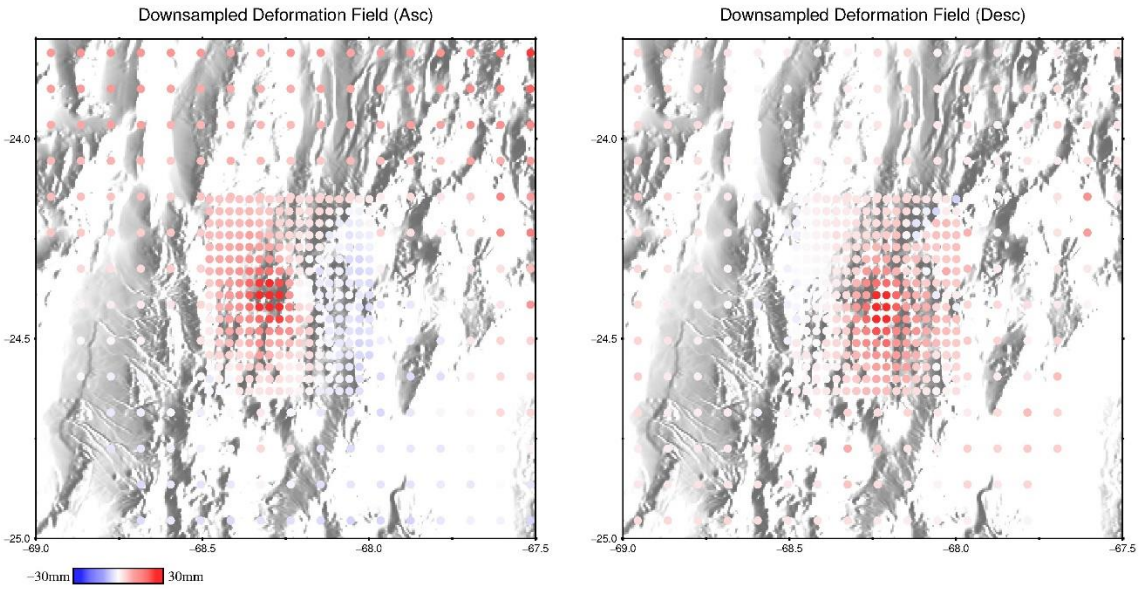

Figure S3. Uniform downsampling of InSAR data for GBIS input. We use a larger pixel density over the Socompa deformation area, resulting in 485 pixels on both the ascending and descending tracks of data.

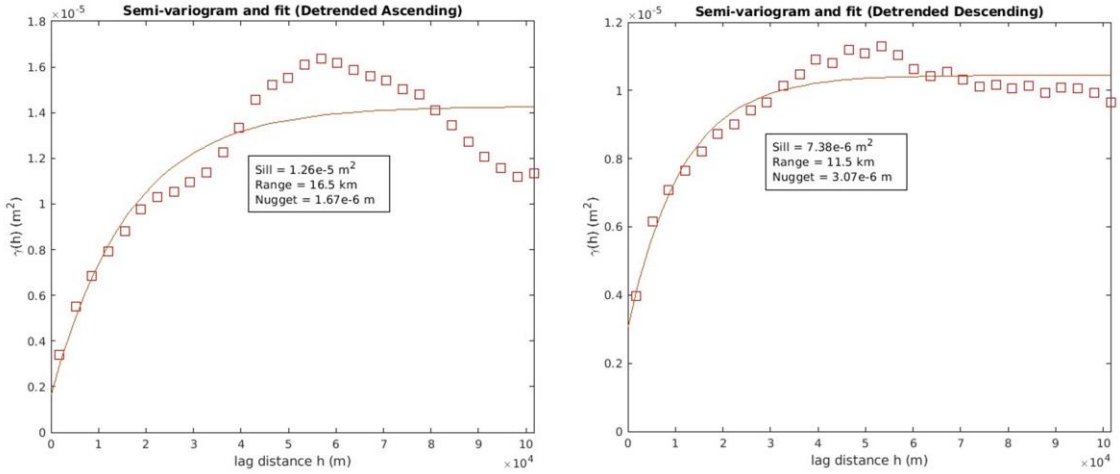

Figure S4. Semi-variogram fitting for post-onset cumulative deformation fields on ascending and descending track using the GBIS software. Errors in the InSAR data can be simulated using an exponential function fitted to the isotropic experimental semi-variogram (Webster & Oliver, 2007), and the lower sill value of the fitted results indicates the higher the signal-to-noise ratio. We use this semi-variogram fitting to calculate the covariance matrix of the InSAR data during the inversion. While for the GPS data covariance matrix, it is obtained from the standard deviations by fitting the equation 2 in the main text.

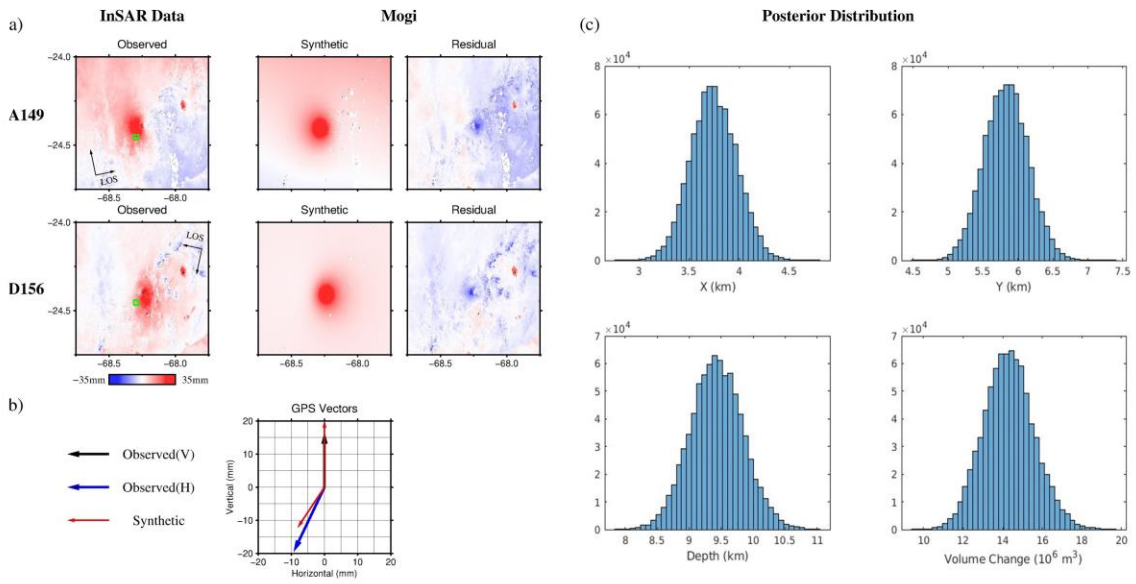

Figure S5. Volcanic source model of Socompa cumulative uplift (Dec 2019 – Oct 2021) using the Mogi model. (a) Modelling results of InSAR observations. The green box indicates the location of the SOCM site. (b) Modelling results of GPS observations. The black vertical vector represents the up component of GPS deformation (~15 mm), while the blue vector signified the horizontal deformation in the east and north directions (here moving ~10 mm west and ~20 mm south). (c) Posterior distributions for all parameters, where X, Y, and Depth indicate the source location reference to the SOCM site (northeast direction), and V represents the volume change (here ~1.4×10^7 m^3).

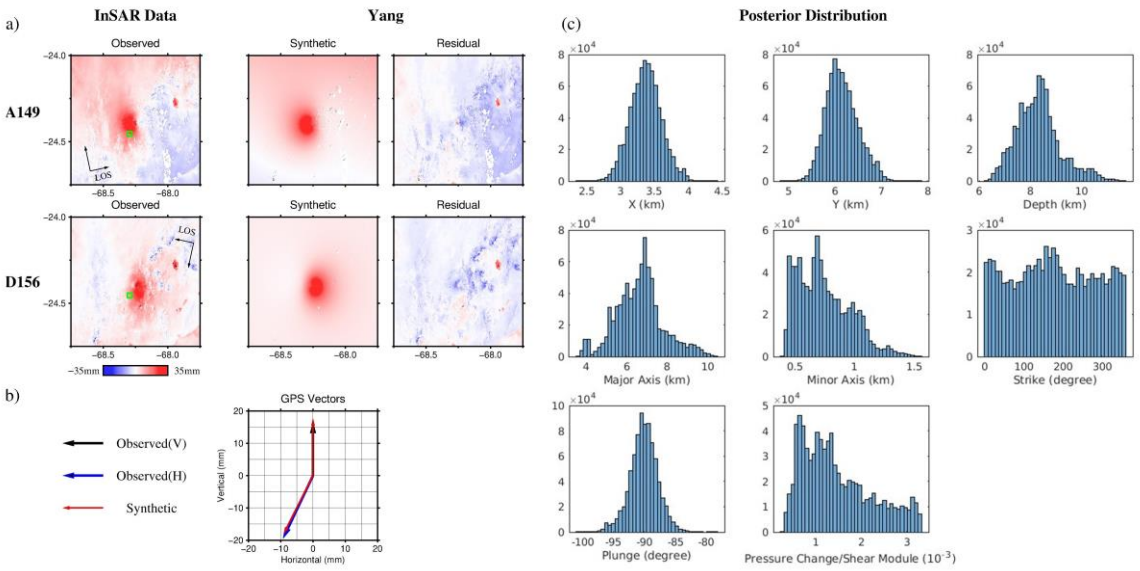

Figure S6. Same as Figure S5 but using Yang model. (c) Semi-major and Semi-minor are the lengths of the two axes, Strike value is the angle of major semi-axis with respect to North, and the Plunge value is the inclination angle of major semi-axis with respect to horizontal. The volume change of the Yang model is ~1.6×10^{7} m^3.

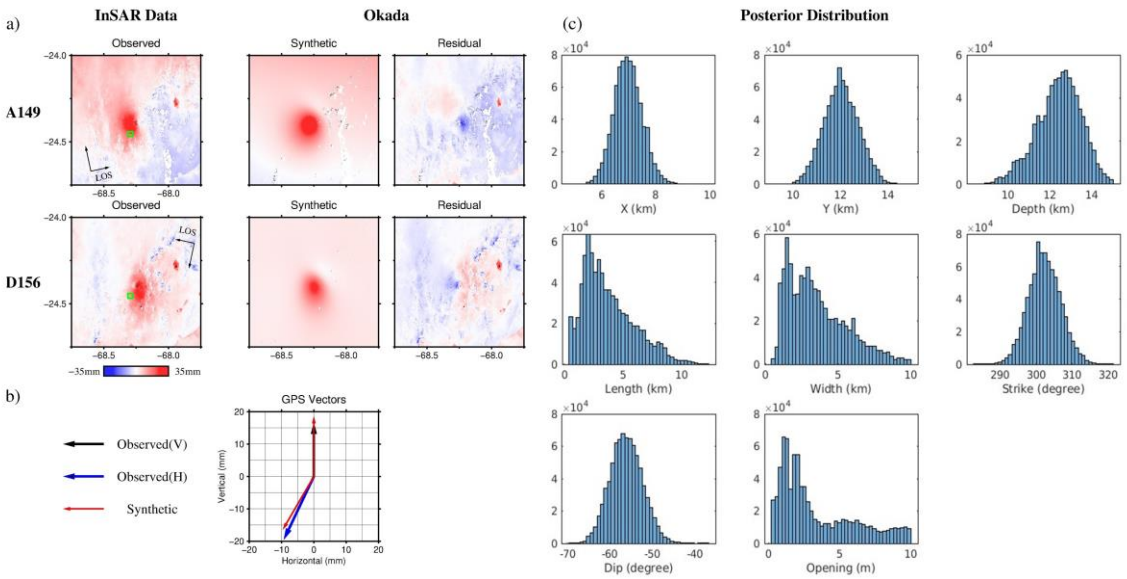

Figure S7. Same as Figure S5 but using Okada model. The volume change of the Okada model is ~2.2×10^7 m^3.

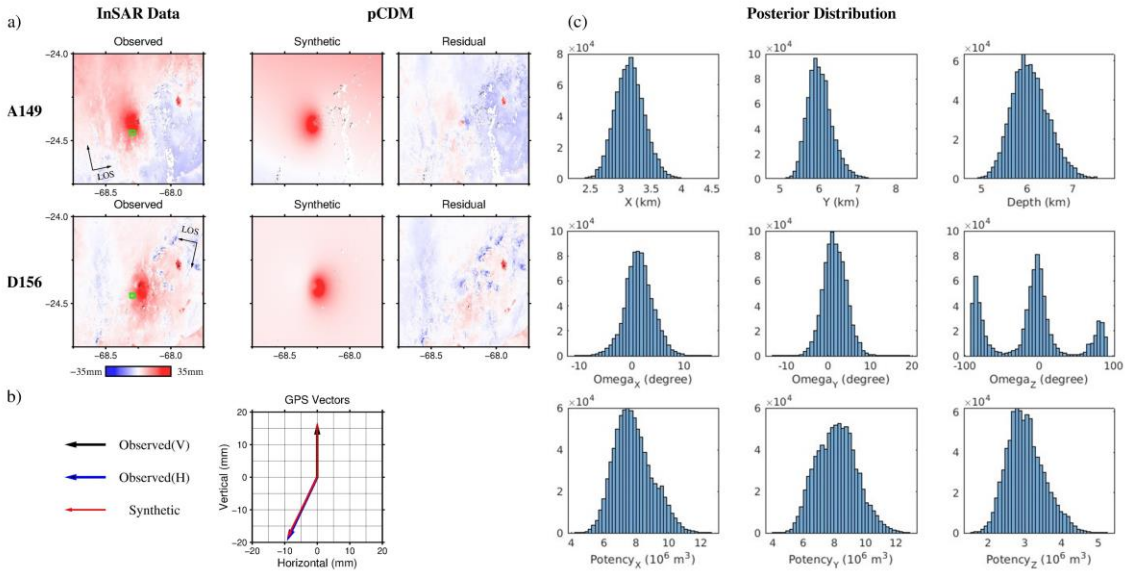

Figure S8. Same as Figure S5 but using pCDM model. (c) Omega$_{X, Y, Z}$ are the rotation angles around three axes, and Potency$_{X, Y, Z}$ are the potencies of the point dislocations on three directions, respectively. Here the bimodal distribution of the rotation angles around the Z axes indicates similar values of potency in the X and Y direction. The total potency of the pCDM, which is defined as the product of dislocation surface area and opening and is a totally different concept from volume change, is ~1.8×10^7 m^3 by summing the potency values in three directions.

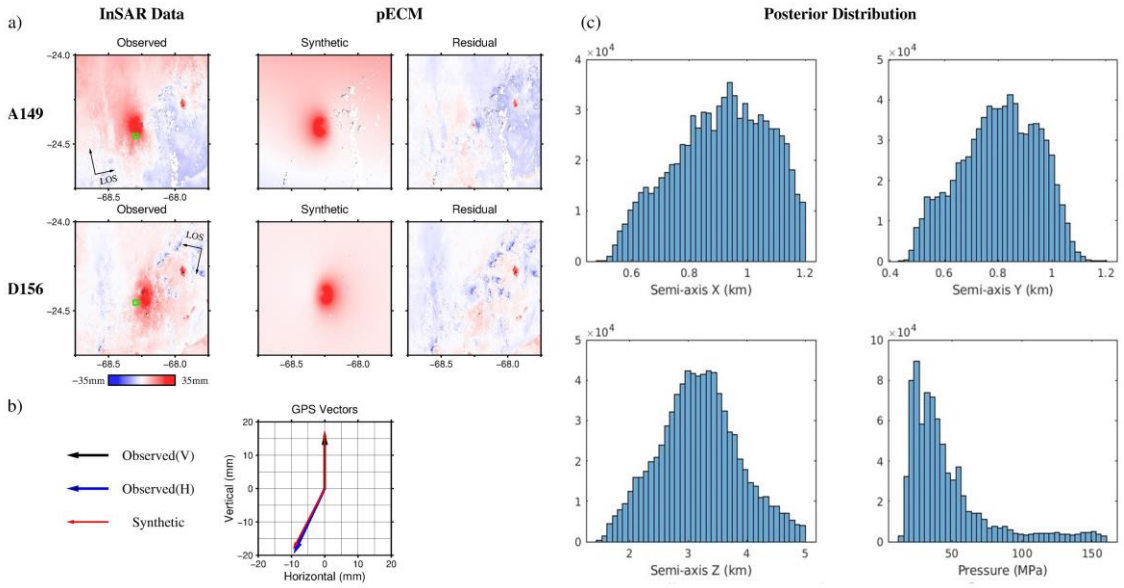

Figure S9. Same as Figure S5 but using pECM model. We use the inferred source location and orientation from pCDM to perform the inversion. The total potency and volume change of the pECM are ~1.8×10^7 m^3 and ~1.1×10^7 m^3, respectively.

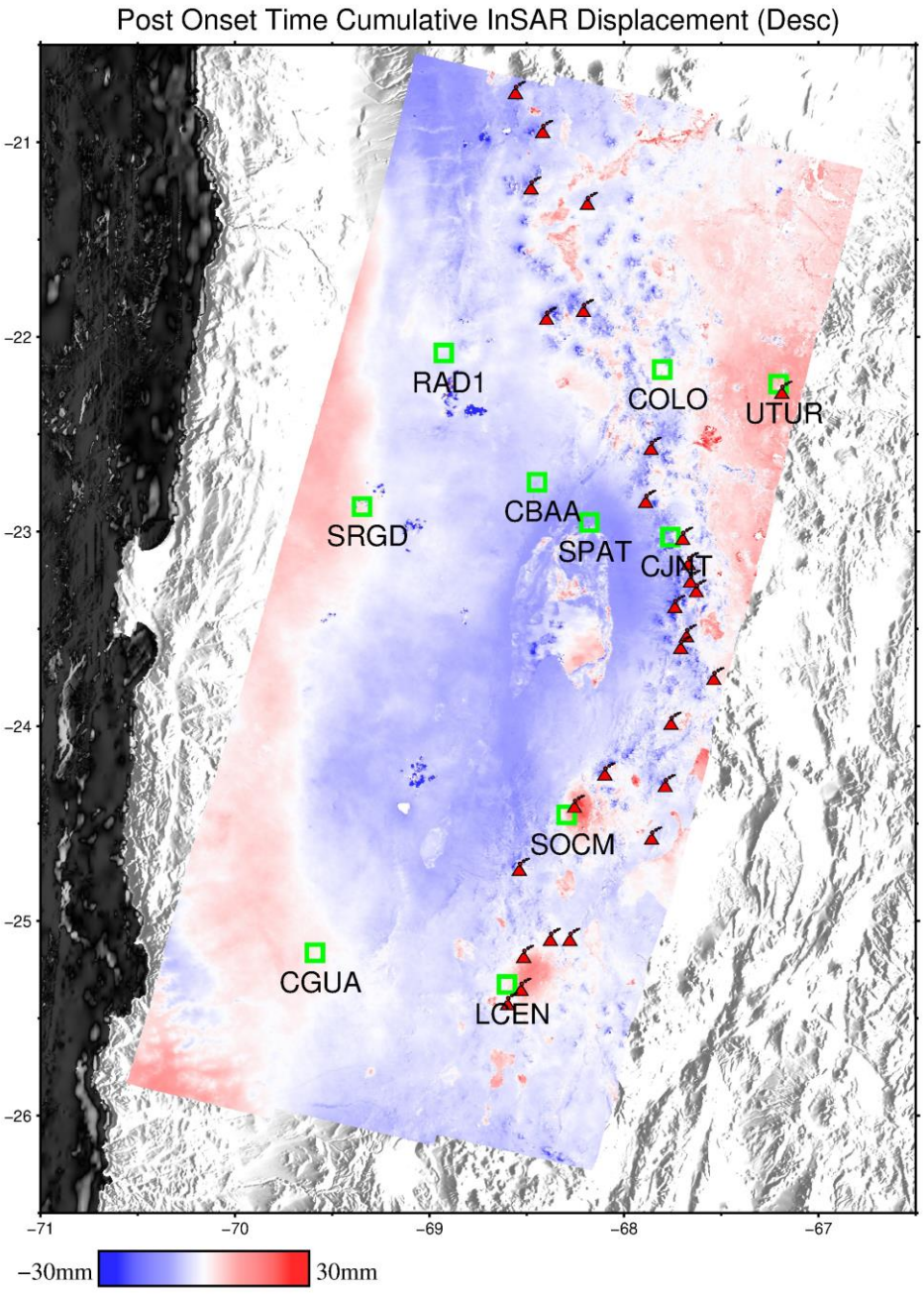

Figure S10. The locations of continuous GPS sites that were used to tie InSAR data, using the descending post onset time cumulated deformation field and topography map as the background image. All GPS data are obtained from the database of the Nevada Geodetic Laboratory.

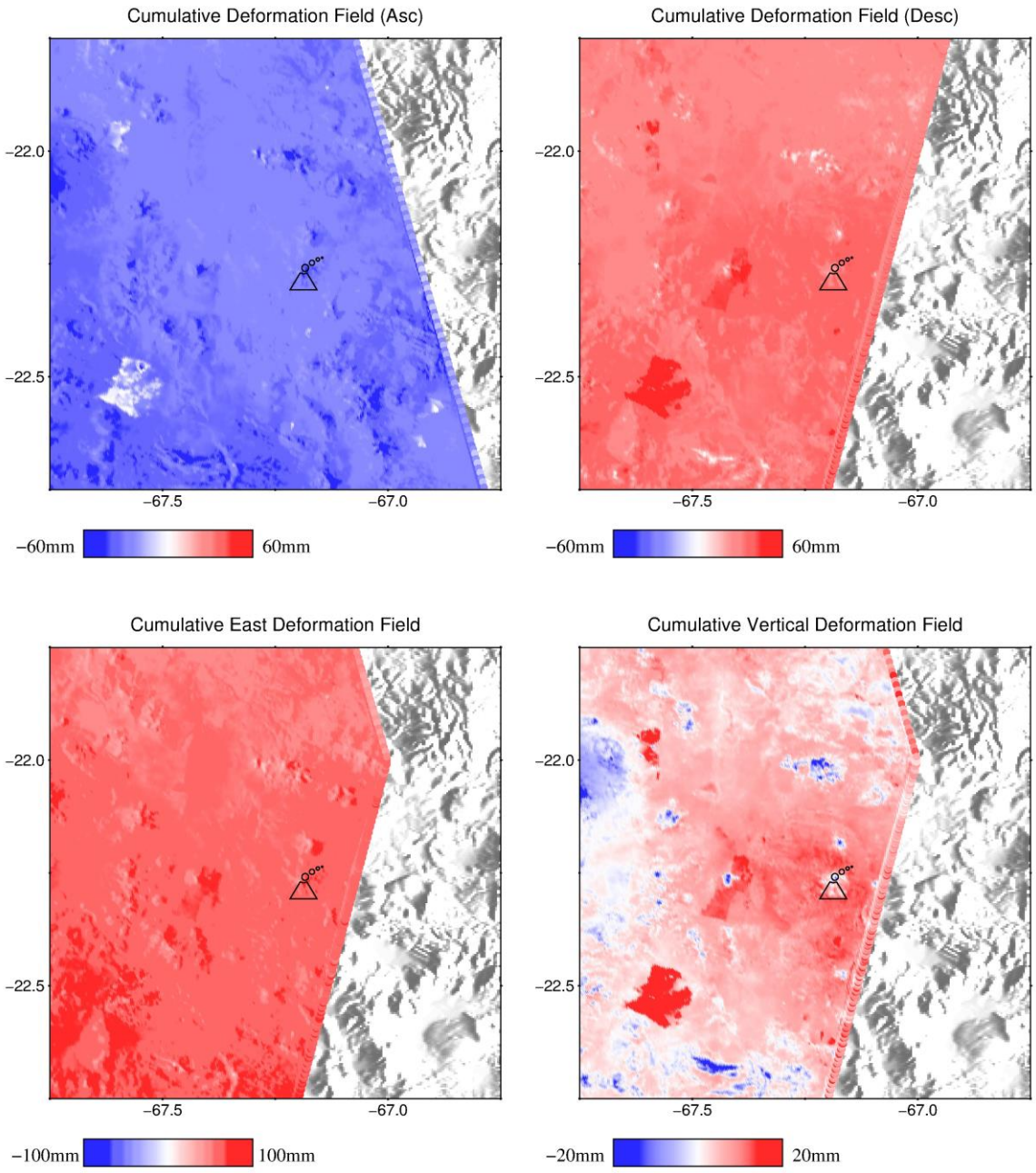

Figure S11. The decomposition of ascending and descending cumulative deformation field (Jan 2018-Oct 2021) into east and vertical deformation field, near the Uturuncu volcano. The ascending and descending cumulative deformation fields are obtained by fitting the whole observation period with one linear velocity.

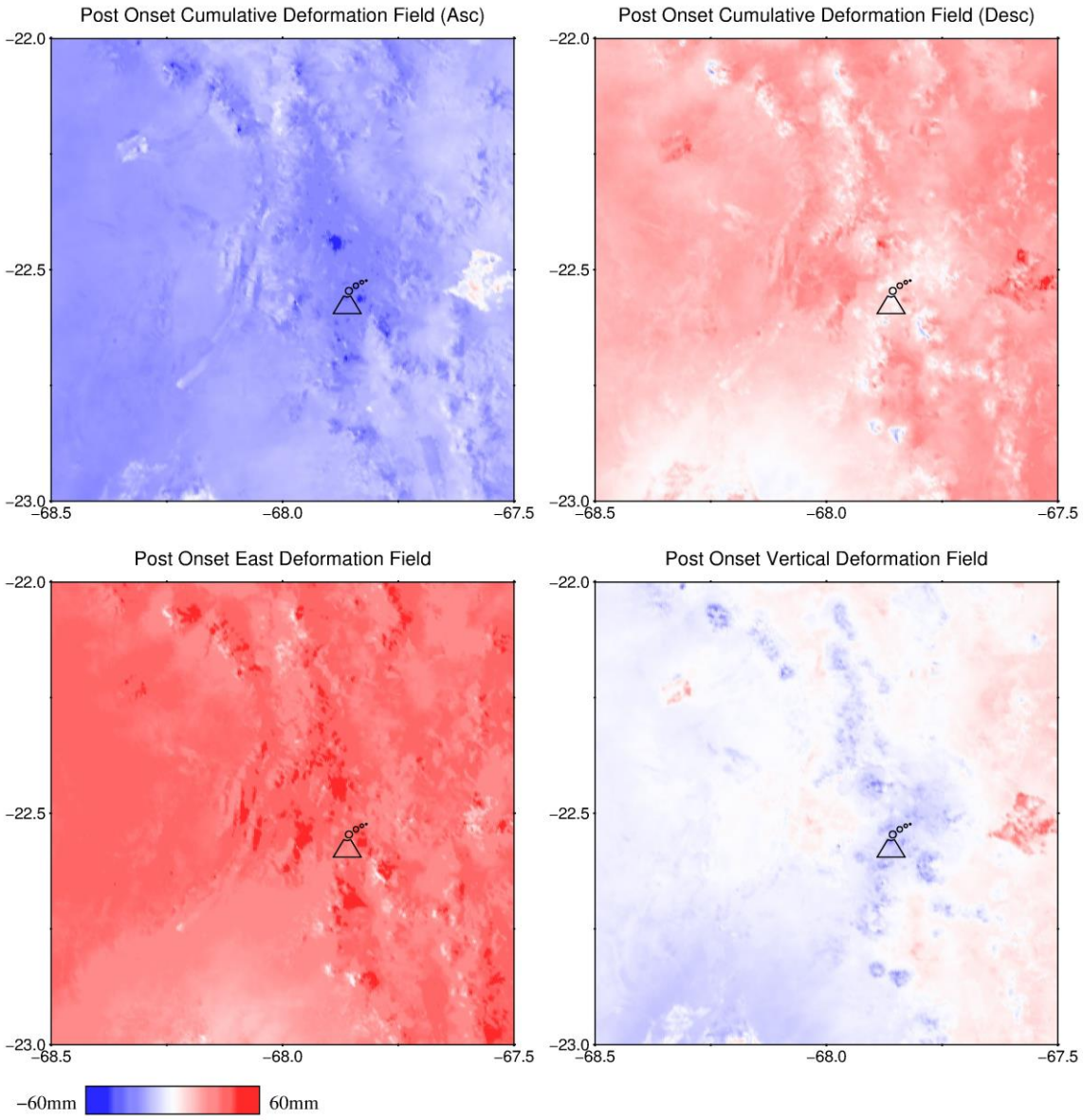

Figure S12. The decomposition of ascending and descending post onset time cumulative deformation field (Dec 2019-Oct 2021) into east and vertical deformation field, near the Putana volcano. The ascending and descending cumulative deformation fields are obtained by fitting equation 1 in the main text.

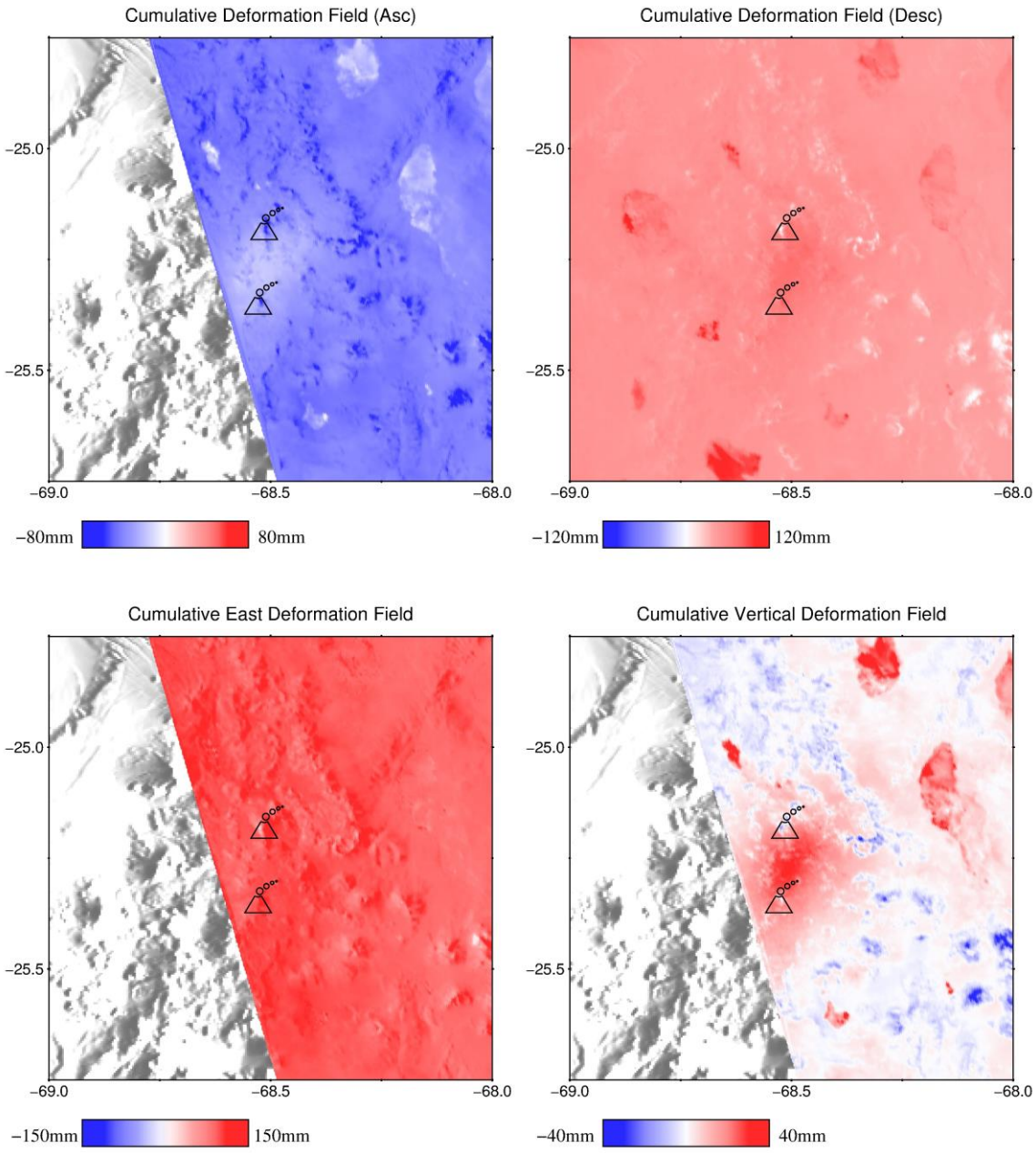

Figure S13. The decomposition of ascending and descending cumulative deformation field (Jan 2018-Oct 2021) into east and vertical deformation field, near the Lazufre (Lastarria & Azufre) volcano. The ascending and descending cumulative deformation fields are obtained by fitting the whole observation period with one linear velocity.

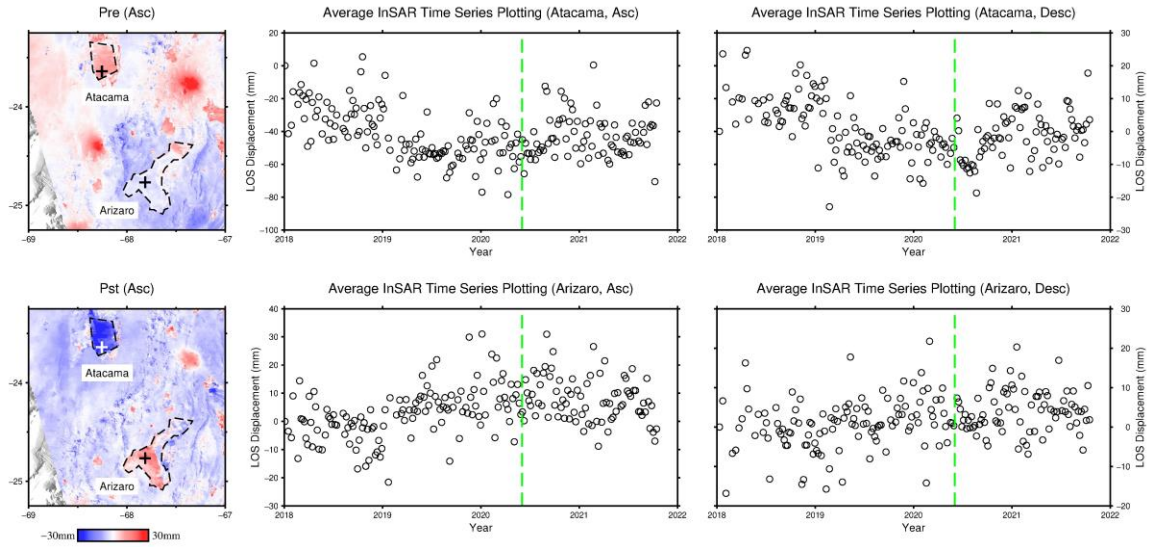

Figure S14. Average InSAR time series over Salar de Arizaro and Atacama region on ascending and descending tracks data. Black dashed polygons, plus symbols, and green dashed lines indicate the approximate boundaries of Salar regions, the location of pixels plot on the time series panels, and the event time of earthquake M_w 6.8, respectively. It shows opposite surface displacements occurrence on Salar de Arizaro and Atacama at the beginning of 2019.

	Mogi	Yang	Okada	pCDM (pECM)
X (km)	3.78	3.56	6.70	3.19
	3.30-4.19	2.94-3.85	5.99-8.05	2.71-3.65
Y (km)	5.71	6.50	11.5	5.82
	5.22-6.44	5.56-6.90	10.6-13.5	5.50-6.77
Depth (km)	9.40	9.85	12.9	5.74
	8.60-10.3	6.83-10.4	10.2-14.3	5.35-6.96
Volume Change ($\times 10^7$ m^3)	1.41	1.61	2.18	1.07
	1.19-1.69	1.04-1.80	1.83-2.95	0.98-1.14

Table S1. The comparison of some main parameters from different volcanic geodetic source modelling results. The optimal values and corresponding 95% confidence intervals are provided. Here X and Y represent the location reference to the SOCM station, where positive values mean towards north or east.

Volcano Name	Monitored or Not	Fumarolic Active	Geodesy Observation	Deformation mechanism and Source Depth	Key References
Ututuncu	N	Y	InSAR from ERS, ENVISAT, Sentinel-1 (1992-2018), GPS	Magmatic. Modelled by several source types, the typical depth is 15-30 km.	Fialko & Pearse, 2012 Henderson & Pritchard, 2017 Gottsmann et al., 2017 Lau et al., 2019 Barone et al., 2019
Putana	N	Y	InSAR from ERS and ENVISAT (1992-2011)	Hydrothermal. A shallow Mogi source at 1 km depth	Henderson & Pritchard, 2013
Lascar	Y	Y	InSAR from ERS, ENVISAT, and TerraSAR-X (1992-2000, 2012-2017), GPS	Complex deformation. A combination of ongoing crater evolution processes, including gravitational slumping, cooling and compaction of eruption products, as well as possible piston-like subsidence	Pritchard & Simons, 2002 Pavez et al., 2006 Richter et al., 2017
Cerro Overo	-	-	InSAR from ERS and ENVISAT (1992-2011)	Controlled by a single reversible mechanism involving fluid accumulation and loss within the crust at ~10 km depth	Henderson & Pritchard, 2013
Lastarria & Azufre	Y	Y	InSAR from ERS, ENVISAT, RADARSAT-2, TerraSAR-X, COSMO-SkyMed, and Sentinel-1 (1995-2016), GPS	Magmatic. Modelled by several source types, the typical depth is <10 km.	Pearse & Lundgren, 2013 Henderson et al., 2017 Díaz et al., 2015

Table S2. Summary of volcanoes in our study area that have been reported to be deforming in the past few decades from previous studies. It shows whether the volcanoes have been monitored by ground observations. Here Cerro Overo presents a deformation area rather than a specific volcano and thus is not marked.